

A Cellular Automation for Real-Time Electrolyte Wetting Simulation in Multilayer Lithium-Ion Cells: From Lab Data to Full-Scale Formats

Nicolaj Kaden, Jincai Cheng, Benjamin Schumann, Do Minh Nguyen,* Ricarda Schlimbach, and Klaus Dröder

Electrolyte filling is a critical step in lithium-ion battery manufacturing, with direct relevance for wetting dynamics, ion transport pathways, and overall cell performance. Despite its significance, modeling approaches capable of reliably capturing electrolyte infiltration in porous electrode-separator composites (ESCs) vary widely in scope, resolution, and applicability. Based on a literature review on modeling and simulation publications in electrolyte filling, a 2D cellular automaton approach is selected for its combination of computational efficiency, parallelization capability, and modeling flexibility. The resulting model simulates capillary-driven electrolyte wetting using experimentally derived material parameters and is validated against tensiometer-based wetting data.

A dynamic time-stepping scheme and saturation-based logic enable accurate predictions at low computational cost. The model reproduces wetting behavior in both single-layer and multilayer ESCs, with strong alignment to experimental data when material interactions are included. Simulations of full pouch and cylindrical cells with varying geometries demonstrate the method's robustness. Across all tested configurations, simulation runtimes remain significantly below physical wetting times, supporting real-time integration. Future work might explore the extension to 3D systems and analysis of design- and process-induced variations in wetting behavior.

1. Introduction

Global warming stands as one of the most pressing issues of our time, necessitating immediate and effective interventions to mitigate its impact.^[1,2] A crucial strategy in this endeavor is the reduction of carbon dioxide emissions, which can be significantly decreased through the widespread substitution of fossil fuels with renewable energy sources.^[1] Central to this transition is the use of batteries as enablers for a sustainable energy infrastructure.^[3–5]

The successful implementation of battery technologies hinges on several key factors, including enhancements in battery

capacity, safety, and reliability.^[6] Advances in these areas have been driven predominantly by breakthroughs in battery materials.^[7,8] Additionally, the cost reduction of batteries is also essential and can be achieved through improvements in the production processes and the exploitation of economies of scale.^[9,10]

Currently, production costs represent about 60%–72% of the total battery costs,^[11–14] with these expenses distributed across different stages of the manufacturing processes: electrode fabrication (24%–33%), cell assembly (35%–38%), and cell finishing (31%–38%).^[15–17] Each step in the production chain adds value and incurs costs, with the latter stages, such as electrolyte filling and cell formation, having a particularly significant impact on the overall cost structure.^[18]

During the electrolyte filling process, the liquid electrolyte must be dispensed into the cell's dead volume to homogeneously wet the pores of the electrode and separator materials.^[19] This is essential for ensuring uniform lithium-ion transport across the electrode surface, preventing defects such as lithium plating during cell formation.^[20,21] However, there are substantial gaps in the current understanding of the product-process relationships at both the material and cell levels during electrolyte filling, but this knowledge is required to achieve the most homogeneous wetting possible.^[18,19]

Recent research has focused on addressing these gaps by investigating various process parameters (e.g., temperature, evacuation pressure, and amount of electrolyte) and product parameters (e.g., electrode materials, separator materials, and material modifications).^[19] These experimental studies, though insightful, are very time-consuming and costly.^[22] Consequently, there is a

N. Kaden, J. Cheng, B. Schumann, D. M. Nguyen, K. Dröder
Institute of Machine Tools and Production Technology
Technische Universität Braunschweig
Langer Kamp 19b, 38106 Braunschweig, Germany
E-mail: do-minh.nguyen@tu-braunschweig.de

N. Kaden, B. Schumann, D. M. Nguyen, K. Dröder
Battery LabFactory
Technische Universität Braunschweig
38106 Braunschweig, Germany

R. Schlimbach
Faculty of Management
Hochschule Heilbronn
Ziegeleiweg 4, 74523 Schwäbisch Hall, Germany

 Supporting information for this article is available on the WWW under <https://doi.org/10.1002/batt.202500356>

 © 2025 The Author(s). *Batteries & Supercaps* published by Wiley-VCH GmbH. This is an open access article under the terms of the Creative Commons Attribution License, which permits use, distribution and reproduction in any medium, provided the original work is properly cited.

growing emphasis on developing virtualized models to describe and predict the filling and wetting behavior of electrolytes more efficiently.^[23]

Table 1 provides an overview of existing models in the literature addressing filling and wetting processes. The investigation of electrolyte wetting behavior in battery electrodes has revealed three primary modeling approaches: the Lattice Boltzmann (LB) method, machine learning (ML) models, and physical-analytic models. Each approach offers unique insights and advantages for understanding and optimizing this key aspect for the resulting battery performance. In the following, we provide a brief overview of the main studies for the respective modeling approaches to then derive our own model that aims for scalable simulation of large systems with localized update rules, seamless parallel computing integration, and high flexibility in modeling complex physical phenomena.

1.1. Lattice Boltzmann (LB)

The LB method simulates complex flows in porous media by employing a molecular description of fluid dynamics. Unlike traditional computational fluid dynamics methods, LB methods utilize lattice points rather than body-fitted meshes, facilitating efficient implementation of unstructured grids and complex geometries. The method probabilistically models particle dynamics through the Boltzmann equation, accounting for convection, external forces, and collisions. These models offer high spatial resolution insights into flow and wetting behaviors within pore structures, thereby aiding in the analysis of process parameters on electrode production.

Studies utilizing LB method, such as those conducted by Jeon et al. have explored the wetting behavior of porous electrodes, demonstrating that factors such as contact angle, calendering, and particle size significantly influence wettability. In particular, Jeon et al. investigated the effect of the active material mixing ratio and particle size distribution, showing that optimized combinations can enhance pore connectivity and accelerate liquid penetration.^[24,25] The influence of electrode compression—the calendering process—was addressed by Lee and Jeon,^[26] where increased densification was shown to reduce wettability by altering pore structure. Further, pore-scale modeling of electrolyte flow in realistic 3D geometries highlighted the role of tortuosity and pore-throat architecture.^[27,28] More recently, the introduction of ceramic-coated separator layers was found to enhance wetting dynamics due to capillarity-promoting surface features.^[29]

Studies by Wanner and Birke have focused on the wetting behavior of lithium-ion battery components with particular emphasis on the interaction between anode and separator materials, highlighting the importance of the material interface for liquid transport. In their earlier work, they demonstrated that the interface between the anode and separator significantly accelerates the wetting front compared to isolated anode structures.^[30] Subsequent studies addressed the influence of surface roughness and electrode structure on local wetting performance,^[31] as well as the effect of mechanical compression after cell winding on electrolyte infiltration.^[32] Most recently, they extended their investigation to include temperature and pressure effects, showing their relevance for

optimizing wetting times under practical cell manufacturing conditions.^[33] These studies combine LBM simulations with experimental visualization methods and modeling approaches, offering a multi-scale perspective on electrode-separator wetting.

Lautenschlaeger et al. studied intramaterial wetting in cathode structures, showing that pore size significantly affects local wetting dynamics.^[22] To reduce computational effort while preserving structural features, they also proposed a homogenized LBM approach for multiphase flow in heterogeneous porous media.^[34]

Shodiev et al. developed advanced 3D-resolved LB models to simulate electrolyte infiltration in complex electrode and separator assemblies. They introduced a multiphase model capable of resolving pore-scale transport across composite structures, revealing the importance of local heterogeneity and interfacial resistance between materials.^[35] Their follow-up work focused on architecture design, showing how gradual porosity gradients and layered electrode structures can significantly accelerate wetting and improve saturation uniformity.^[36]

Abubaker et al. investigated electrolyte wetting at interfaces between electrode, separator, and current collector materials, focusing on the influence of calendering and contact angles. In their initial study, they systematically varied the calendering degree and contact angles to quantify their impact on saturation times and gas entrapment.^[37] A follow-up work emphasized the role of localized interface phenomena, highlighting the sensitivity of electrolyte penetration to variations in current collector interactions.^[38] In their most recent publication, they extended the analysis to layered NMC electrodes with spatially resolved porosity distributions, revealing interface-specific effects on gas trapping and local saturation heterogeneity.^[39]

Additionally, Mohammadian and Zhang investigated the impact of microchannels on porous electrode wettability. Their findings indicate that smaller and more numerous microchannels substantially enhance electrolyte transport into the porous structure by reducing local capillary barriers and facilitating rapid infiltration across the electrode thickness.^[40]

Chen et al. reconstructed realistic 3D electrode microstructures from synchrotron X-ray tomography and performed LB simulations to analyze how calendering pressure and active material fraction jointly influence permeability and capillary-driven wetting dynamics.^[41] Chen et al. used 4D visualization and pore-scale modeling to quantify inhomogeneous electrolyte wetting, highlighting how spatially varying structures lead to localized wetting delays and incomplete saturation.^[42] Cho et al. applied a color-gradient LB method to simulate gas–liquid transport in porous structures, with a particular focus on trapped air behavior and its influence on oxygen diffusion. Their results reveal that wettability, more than porosity or viscosity ratio, governs the extent of gas entrapment and therefore strongly impacts transport efficiency in porous electrodes.^[43]

While these LB-based approaches provide valuable pore-scale insights and capture complex interfacial dynamics, they are typically associated with high computational costs and long runtimes in the range of hours. This limits their applicability for inline process monitoring and real-time quality control, particularly in large-format cells or full electrode-separator composites (ESCs).

Table 1. Overview of publications with modeling and simulations in electrolyte filling with classification into different categories.

Studies	Model properties					Observation level					Investigated materials						
	Model type	Dimension	Validation	Outcome	Dispensing	Wetting	Pore level	Cell level	Process level	Cell type	Intra			Inter			
											A	C	S	A + S	C + S	A + S + C	Cell stack
Abubaker et al. 2024a ^[39]	LB	2D	AC	SA		X	X				X	X					
Abubaker et al. 2024b ^[38]	LB	2D	AC	SA		X	X							X	X		
Abubaker et al. 2024c ^[37]	LB	2D	AC	SA		X	X							X	X		
Chen et al. 2023 ^[42]	LB	2D	EX	WD		X		X			P			X			X
Chen et al. 2025 ^[41]	LB	3D	AC	WD		X	X							X			
Cho et al. 2022 ^[43]	LB	3D	EX	SA		X	X							X			
Davoodabadi et al. 2019 ^[54]	MA	1D	EX	WD		X	X							X	X		
Dent et al. 2024 ^[49]	MA	2D	EX	SA		X	X	X			H						X
El Malki et al. 2023 ^[44]	ML	3D	CV	SA		X	X							X			
Gebrekirros Berhe et al. 2023 ^[55]	MA	1D	EX	WD		X	X							X			
Günter et al. 2021 ^[58]	MA	2D	EX	SA		X		X			H						X
Günter et al. 2022 ^[72]	EC	1D	EX	CP		X		X			HC						X
Hagemeister et al. 2022 ^[73]	FE	3D	EX	VF	X	X		X			H						X
Hagemeister et al. 2024a ^[60]	FE	3D	EX	WD		X	X	X			PH	X	X				X
Hagemeister et al. 2024b ^[23]	FE	3D	EX	WD	X	X	X	X			P	X					X
Jeon 2016 ^[24]	LB	2D	AC	SA		X	X							X	X		
Jeon 2019 ^[27]	LB	2D	AC	SA		X	X							X	X		
Jeon 2021 ^[25]	LB	2D	AC	SA		X	X							X		X	
Jeon et al. 2022 ^[29]	LB	2D	EX	SA		X	X							X		X	
Knoche et al. 2016 ^[74]	GM	1D	CL		X	X			X		PH						
Lautenschlaeger et al. 2022a ^[34]	LB	3D	AC	SA		X	X							X			
Lautenschlaeger et al. 2022b ^[22]	LB	3D	AC	SA		X	X							X		X	
Lee & Jeon 2014 ^[26]	LB	2D	AC	SA		X	X							X	X		
Lee et al. 2013 ^[28]	LB	2D	AC	SA		X	X								X		
Mohammadian & Zhang 2018 ^[40]	LB	2D	AC	SA		X	X							X	X		
Neumann et al. 2016 ^[61]	FE	3D	AC	VF		X		X			P						X
Neumann et al. 2017 ^[50]	MA	1D	AC	WD	X	X		X			P						X
Sauter 2020 ^[51]	MA	3D	EX	SA		X	X							X			
Schnell 2019 ^[47]	ML	1D	EX	CP	X	X		X			PH						X
Schönemann et al. 2019 ^[48]	ML	1D	CL	CP		X		X									X
Shin et al. 2022 ^[52]	MA	3D	EX	SA		X	X							X	X		

Table 1. Continued.

Studies	Model properties					Observation level					Investigated materials						
	Model type	Dimension	Validation	Outcome	Dispensing	Wetting	Pore level	Cell level	Process level	Cell type	Intra			Inter			
											A	C	S	A + S	C + S	A + S + C	Cell stack
Shodiev et al. 2021a ^[45]	ML	3D	CV	SA		X	X							X	X		
Shodiev et al. 2021b ^[35]	LB	3D	EX	SA		X	X								X		
Shodiev et al. 2022 ^[36]	LB	3D	EX	SA		X	X							X	X	X	X
Stock et al. 2022 ^[46]	ML	1D	CV	CP		X		X						P			X
Usseglio-Viretta et al. 2023 ^[53]	MA	2D	CL			X		X				P	X				
Wanner & Birke 2022 ^[30]	LB	3D	EX	SA		X	X							X		X	
Wanner & Birke 2023 ^[31]	LB	3D	EX	SA		X	X							X		X	
Wanner & Birke 2024a ^[32]	LB	3D	EX	SA		X	X							X	X	X	
Wanner & Birke 2024b ^[33]	LB	3D	EX	SA		X	X							C	X		
Wanner et al. 2023 ^[56]	MA	1D	CL	WD		X		X				H	X	X	X		
Wood et al. 2015 ^[9]	MA	1D	CL	CO		X		X				P					

Model type.

MA = Mathematical-analytical model.

LB = Lattice Boltzmann model.

FE = Finite elements/volume method.

EC = Electrochemical model.

ML = Machine learning model.

GM = Graphical model.

Validation method.

AC = Analytical calculation.

EX = Results of experimental tests.

CV = Cross-validation with validation data set.

CL = Comparison with other literature models.

Simulation outcome.

SA = Saturation.

VF = Electrolyte volume fraction.

WD = Wetting degree.

CP = Cell performance.

CO = Cell cost.

Cell type.

P = Pouch.

H = Hardcase.

C = Coin/Cylindrical.

1.2. Machine Learning (ML)

ML models are algorithmic systems used to learn and recognize patterns in data, making predictions based on input parameters. In the context of battery electrodes, ML models optimize wettability during the electrolyte filling process. By analyzing factors such as electrolyte composition, temperature, and pressure, ML algorithms can recommend suitable conditions for electrolyte infiltration into porous structures. These models can range from macroscopic process parameters to microscopic interactions, providing insights that can lead to process adjustments for improved wettability.

Elmalki et al. investigated the influence of manufacturing parameters—particularly calendaring degree—on electrolyte

infiltration in lithium-ion batteries, using LB simulations to train a surrogate ML model for efficient and low-cost wetting prediction.^[44] Shodiev et al. introduced an ML model using the multi-layer perceptron approach to predict electrolyte flow and wetting in battery electrodes. Trained on a 3D LB method database, this model offers accurate, low-cost predictions, enabling large-scale optimization of electrode structures.^[45] Stock et al. applied ML for early quality prediction in lithium-ion battery production. By using regression models and neural networks to analyze inline measurement data such as electrode thickness, coating weight, and calendering pressure, they achieved high accuracy in predicting cell quality and classifying cycle life groups, enhancing electrolyte wetting process efficiency.^[46] Schnell et al.

employed data mining techniques to identify key quality drivers in the electrolyte filling process of lithium-ion battery production. By analyzing variables such as electrode thickness, porosity, and electrolyte viscosity, they utilized models including Generalized Linear Models, Random Forests, and Gradient Boosted Trees to predict battery cell capacities. This approach enabled the reduction of production costs and scrap rates.^[47]

Despite their predictive power and speed, ML models are often reliant on large, high-quality training datasets and do not inherently incorporate physical causality. As a result, their use in exploratory process optimization or in novel material systems remain limited, especially in contexts requiring physical interpretability or extrapolation beyond trained regimes.^[45,46,48]

1.3. Mathematic-Analytic (MA)

MA models integrate physical laws with mathematical techniques to predict phenomena, prioritizing interpretability over numerical complexity. They utilize closed-form solutions, employing differential equations and mathematical tools to analyze fluid mechanics. Common equations such as Hagen–Poiseuille's law, the Young–Laplace equation, and Darcy's law form the basis of these models,^[49–53] with variants such as the Lucas–Washburn equation (LWE)^[54–56] and models by FRIES^[57] offering insights into the temporal spread of a liquid in a porous solid. Dent et al. critically reviewed the applicability of these approaches in battery manufacturing, emphasizing both their relevance and their limitations in capturing complex pore networks.^[49] Gebrekirnos Berhe et al. applied a Washburn-based framework to quantify the influence of laser-induced surface grooves on wetting behavior.^[55] Gunter et al. combined analytical modeling based on the equation by FRIES with experimental validation to assess the impact of pressure and temperature on infiltration dynamics.^[58] The mathematical relationships serve as a parameterization basis in experimental studies, aiding in determining wetting constants like penetration or wetting rates. However, these models are generally limited to idealized geometries and homogeneous materials. They lack the spatial resolution to capture structural effects at the component level and cannot resolve local heterogeneities or interfacial phenomena in multilayer configurations sufficiently.

1.4. Further Models

Hagemeister et al. developed finite volume models to analyze the effects of pressure and temperature, verified by neutron radiography, and provided recommendations to enhance wetting and reduce production costs in larger-format cells.^[59] In a subsequent study, they coupled pore-scale permeability calculations with ANSYS-based CFD simulations to simulate the entire filling process across different cell types, demonstrating the applicability of the model to varying geometries and operating parameters.^[60] In their most recent publication, they validated the model with

experimental neutron radiography data for hardcase and pouch cells and highlighted the sensitivity of wetting dynamics to evacuation pressure and electrolyte temperature, supporting the use of simulation-based optimization for industrial process integration.^[23]

Neumann et al. developed a numerical model using the finite volume method to study the displacing flow at the battery level. Their investigation focused on wall effects and capillary action in porous materials, supported by experiments to determine porosity and key properties affecting two-phase flow, revealing significant impacts on flow characteristics.^[61] While these continuum-based models bridge the gap between pore- and cell-scale simulation, they are typically complex, inflexible, and computationally demanding. Most importantly, they are not designed for high-throughput prediction or fast parameter studies, making them unsuitable for inline-capable process control and decision-making systems.

Despite recent progress in pore-scale modeling, most existing approaches remain limited in scalability and computational efficiency. Their high resolution often comes at the cost of long simulation times, which renders them impractical for integration into real-time production control systems. This is particularly critical in lithium-ion battery manufacturing, where each process step strongly influences downstream operations, and quality deviations can propagate undetected throughout the chain.

To enable responsive and predictive quality management, process models must be embedded into a cross-process control framework capable of adapting to upstream variations. Meiners et al. have demonstrated the potential of such architecture, in which process parameters and intermediate product properties are recorded, analyzed, and used to dynamically adjust subsequent processes. While this existing research did not focus on wetting models specifically, it clearly outlined the structural and functional requirements for inline-capable models that contribute to data-driven decision-making. This highlights the need for efficient, scalable wetting models suitable for integration into holistic production control systems.^[62]

This article aims to showcase the development of such a model, designed for inline prediction of wetting times.

While existing modeling approaches offer specific strengths, they may also face certain limitations in the context of inline application (Table 2). For instance, LB models can provide high-resolution insight into pore-scale dynamics but are often computationally demanding for large-scale predictions. ML approaches may achieve fast inference but can struggle with physical interpretability and extrapolation. MA models are well suited for parameter estimation and conceptual understanding but typically lack the spatial resolution required for complex geometries. The proposed model addresses these challenges by combining scalable simulation for large systems with localized update rules, real-time computational feasibility, and flexible transition logic that can incorporate physically meaningful effects. It is intended to complement existing modeling approaches by enabling efficient integration into production environments, supporting predictive quality management, and real-time adaptation in battery manufacturing.

Table 2. Qualitative assessment of different model types with regard to central requirements for inline-capable wetting models.			
Model type	Efficient for large systems	Real-time capable	Flexible transition logic
LB	●	○	●
ML	●	●	○
MA	●	●	●
FE	○	○	●
EC	○	●	○
GM	○	●	○

○ = limited suitability in typical implementations.
● = partially fulfilled or strongly dependent on application context.
● = well suited for the criterion in many implementations.

For this purpose, the model setup is detailed in the second section "Methods and Simulation Model"; additionally, the experimental setup for the validation is described here. The section "Results and Discussion" is intended to provide an overview of the model validation and the results of the parameter variations. Finally, conclusions are drawn in section "Conclusion" and the further possibilities are briefly outlined.

2. Methods and Simulation Model

2.1. Model Approach

We simulate the temporal evolution of electrolyte distribution within the ESC using a 2D cellular automaton (CA) model. CAs are discrete mathematical systems defined by a fixed set of transition rules, where the state of each cell evolves over time depending on the states of its neighbors.^[63,64] Due to their simplicity, flexibility, and computational efficiency, CA models are well suited and used to describe capillary-driven wetting dynamics in porous media in nonbattery contexts.^[65–67]

The decision to employ a CA approach is motivated by three key advantages: 1) it allows efficient simulation of large systems through localized update rules; 2) it enables real-time computation through discrete updates and straightforward parallelization across spatial domains; and 3) it offers high modeling flexibility, particularly in modifying transition logic to integrate physical effects, such as material-dependent permeability or wetting resistance, or experimental dependencies.

CAs are defined by five main components: grid, neighborhood, state, boundary condition, and transition function. These elements are described in the following and shown in Figure 1 in detail.

The ESC is represented by a 2D grid, each cell of this grid relates to a discrete volume element of the porous domain. The model simplifies the inherently 3D structure by assuming uniform wetting behavior along the through-plane direction. This assumption reduces computational complexity while preserving the essential dynamics of in-plane electrolyte propagation; however, it may slightly underestimate wetting anisotropies or local delays in through-plane infiltration, especially in highly

inhomogeneous or anisotropic materials. Grid discretization is defined in length units (lu) for spatial resolution and time units (tu) for temporal resolution. The spatial grid is surrounded by a boundary layer representing dead volume and allows for different wetting configurations (e.g., one-front, two-front, or four-front injection scenarios).

A Moore neighborhood is applied, so each cell interacts with its eight surrounding cells. This configuration captures the connectivity of pore structures in electrode and separator materials and enables multi-directional capillary flow simulation.

The state of each cell is defined by a continuous value between 0 (dry) and 1 (fully saturated), representing the local degree of pore saturation. Wetting progresses based on the filling level of neighboring cells and the capillary transport potential, which is governed by surface tension, pore radius, viscosity, and contact angle.

Boundary condition defines the interaction of the fluid particles with the boundaries of the computational domain. In this simulation model, the density boundary condition is adapted according to the configuration of the fluid inlet. To approximate the experimental test method of a tensiometer with a single-front in the simulation, the bottom of the model is defined as a constant source inlet with constant density and permanent cell state of 1. The sides with liquid inlets are adapted accordingly for cell wetting—for coiled cells with two sides (top and bottom) and stacked cells with four sides (each side). Unlike the

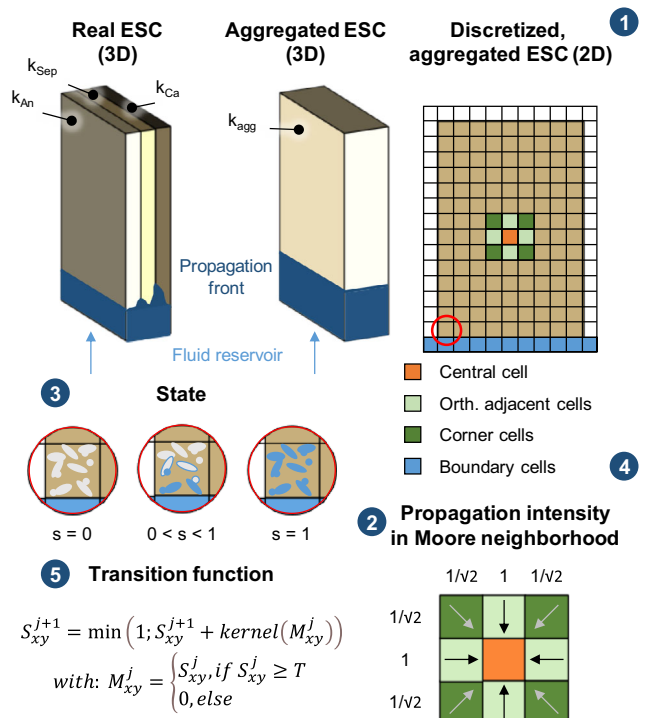


Figure 1. Schematic representation of the CA model used to simulate electrolyte wetting in porous lithium-ion cell components. The model is defined by four core elements: (1) a 2D spatial grid representing the ESC, (2) the Moore neighborhood for local interactions, (3) a continuous state variable indicating local saturation, (4) the boundary condition, and (5) a transition function based on the LWE to capture capillary-driven wetting dynamics.

boundary-back condition usually used in LB method, this model employs an open boundary to simulate the evaporation of the electrolyte at the edges of the electrode sheet.^[68]

The transition function determines the change in saturation for each cell based on its surrounding neighborhood. Each neighboring cell (NC) contributes to the filling of the central cell (CC), depending on 1) the current saturation of the NC, 2) the relative position to the CC (e.g., diagonal or direct neighbor), and 3) the simulation time step.

To model capillary-driven infiltration, the transition function is based on the LWE,^[69] which relates wetting front velocity to material properties (Equation (1))

$$h = k \cdot t^{0.5} \text{ with } k = \sqrt{r_{\text{eff}} \cdot \cos(\theta) \cdot \frac{\sigma}{2\eta}} \quad (1)$$

The LWE-based rule captures the characteristic $\alpha t^{-0.5}$ dependence of wetting front progression and allows for a differentiation between anode, cathode, and separator regions. The LWE's wetting rate k [mm s^{-0.5}] is used as a material-specific parameter and mapped to simulation units via a dynamic time increment $t_{\text{incr}}(j)$ [s·tu⁻¹]. This transformation accounts for the degressive nature of capillary flow over time and ensures consistency between physical and simulation scales.

To account for the directionality of the wetting rate, the 1D flow is expressed as a combination of one orthogonal and two diagonal components. Assuming isotropic material properties, the components can then be expressed as

$$k_{\text{orth}} = \frac{k}{1 + \sqrt{2}} \quad (2)$$

$$k_{\text{diag}} = \frac{k}{2 + \sqrt{2}} \quad (3)$$

The temporal discretization is indirectly controlled by a pre-defined maximum wetting rate k_{max} [lu tu⁻¹], which corresponds to the upper bound of electrolyte propagation per time increment. Based on the discretized LWE, the variable time increment for step j [tu] is calculated as

$$t_{\text{incr}}(j) = \left(\frac{2 \cdot k_{\text{max}}}{k \cdot l_{\text{incr}}} \right)^2 \cdot j \quad (4)$$

Here, l_{incr} is the spatial discretization [mm lu⁻¹], and k is the physical wetting rate of the material. The effective wetting rate in the simulation, $k_{\text{sim}}(j)$ [lu tu⁻¹], for the time step j is then

$$k_{\text{sim}}(j) = \frac{dh_{\text{sim}}}{dt} = \frac{0.5 \cdot k \cdot \sqrt{t_{\text{incr}}(j)}}{l_{\text{incr}}} \cdot j^{-0.5} \quad (5)$$

This ensures that the wetting front decelerates over time in accordance with the physical LWE behavior. The simulated wetting rate k_{sim} is defined at a constant value in relation to the grid size to reduce simulation time. This results in a formula for the absolute time combining (4) and (5)

$$t(j) = \left(\frac{2 \cdot k_{\text{sim}} \cdot l_{\text{incr}}}{k} \right)^2 \cdot \frac{j(j-1)}{2} \quad (6)$$

To reflect partial filling behavior, the influence of a neighbor cell is scaled by its saturation level. For example, a cell filled to 50% can only contribute half of its potential filling strength to its neighbors. Moreover, as each CA cell can only reach a saturation value of 1, any overflow due to excessive inflow is truncated. To minimize numerical loss, a wetting threshold T is introduced: neighboring cells only begin to transfer electrolyte once their own saturation exceeds the defined minimum threshold value T . This model's prepercolation effects observed in porous media and avoids premature lateral propagation.

The threshold is applied using a mask M on the simulated plane. Then, a kernel operator is used to implement the LWE using the directional wetting rates from (2) and (3) in the neighborhood. The resulting transition function describes the current state S_{xy}^j at the grid point (x,y) in simulation step j as follows,

$$S_{xy}^{j+1} = \min(1; S_{xy}^j + \text{kernel}(M_{xy}^j)) \text{ with: } M_{xy}^j = \begin{cases} S_{xy}^j, & \text{if } S_{xy}^j \geq T \\ 0, & \text{else} \end{cases} \quad (7)$$

where M_{xy}^j is the mask which applies the wetting threshold T and kernel is the point operator which applies the LWE in the Moore neighborhood.

The model is implemented in Python, and the simulations are executed on an NVIDIA GeForce RTX 4070 Ti SUPER with 16 GB.

2.2. Simulation Setup and Approach

To ensure accurate and computationally efficient wetting simulations, the CA model requires prior parameterization based on material-specific data. This includes defining the spatial and temporal resolution as well as internal control parameters such as the maximum wetting rate per time increment and the wetting threshold.

2.2.1. Model-Specific Parameterization

The model domain is discretized in space and time using dimensionless units. The spatial resolution is given by the length increment l_{incr} , and the temporal resolution is governed by the time increment $t_{\text{incr}}(j)$, which is dynamically adapted to reflect the degressive nature of capillary-driven flow. The derivation and implementation of $t_{\text{incr}}(j)$ and the corresponding effective wetting rate $k_{\text{sim}}(j)$ are described in detail in the Model Approach section (Equations (4) and (5)).

Since each cell can only accept a limited inflow per time step, both the allowable inflow and tolerable numerical loss are defined as control parameters. Furthermore, a threshold is introduced, determining the minimum saturation level a cell must reach before it can begin to wet neighboring cells. This threshold governs the geometry of electrolyte propagation and affects the model's response near material interfaces.

To establish appropriate values for the spatial resolution l_{incr} , the maximum wetting rate k_{max} , the threshold parameter, and

experimental data from a single reference material (anode A1) are used. The calibration process aims to balance model accuracy and computational runtime by comparing simulation outputs with analytical predictions from the LWE. The quality of the parameterization is later assessed using error metrics such as cumulative deviation and geometric model quality indicators, as described in the results section.

2.2.2. Validation Metrics

To quantify the accuracy of the infiltration during parameterization, a reference comparison is made against the analytical solution of the LWE (Equation (1)). Two complementary error metrics are applied.

Maximum error Err_{\max} : The largest pointwise deviation between the simulation and the reference model

$$\text{Err}_{\max} = \max(|h_{SM}(j) - h_{LWM}(j)|) \quad (8)$$

Cumulative error Err_{cum} : The integrated absolute deviation weighted over simulation time

$$\text{Err}_{\text{cum}} = \sum_{j=0}^{\text{end}} |h_{SM}(j) - h_{LWM}(j)| \cdot \sqrt{t(j)} \quad (9)$$

Here, $h_{SM}(j)$ denotes the simulated wetting height at time step j , and $h_{LWM}(j)$ is the corresponding analytical value. While Err_{\max} is sensitive to local deviations caused by spatial discretization, Err_{cum} provides a more robust, integrated measure of model accuracy. Therefore, the cumulative error is used as the primary evaluation metric in the parameter selection process.

2.2.3. Evaluation Methodology for Model Comparison

To compare the simulation results with experimental measurements, the time-resolved height of the wetting front is used in a tensiometer test. The results of such a test are shown as an example in red in Figure 2.

During the initial phase of measurement ($0-3 \text{ s}^{0.5}$), transient effects such as lamella spreading and edge wetting can lead to deviations not captured by the simulation. Therefore, the quantitative comparison focuses on the stable, linear portion of the curve. We used two model quality (MQ) metrics:

Slope deviation MQ_{slope} : difference between the experimental and simulated slope, relative to the experimental value

$$\text{MQ}_{\text{slope}} = \frac{|k_{\text{exp}} - k_{\text{sim}}|}{k_{\text{exp}}} \quad (10)$$

Offset deviation $\text{MQ}_{\text{offset}}$: absolute vertical offset at the start of the linear regime

$$\text{MQ}_{\text{offset}} = |a_{\text{exp}} - a_{\text{sim}}| \quad (11)$$

Here, k_{exp} and k_{sim} represent the slopes of the experimental and simulated wetting curves, respectively, obtained via linear regression. The parameters a_{exp} and a_{sim} correspond to the

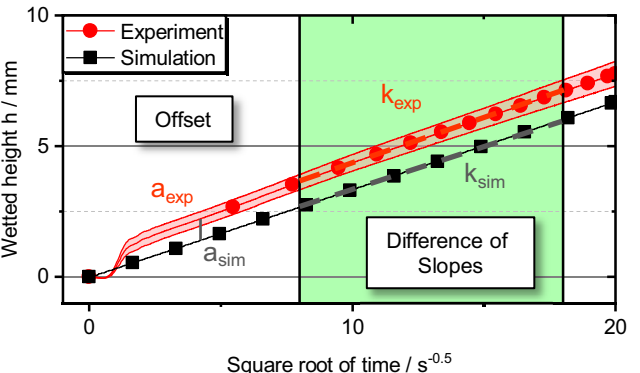


Figure 2. Evaluation method for model quality based on simulated and experimental wetting curves (h vs. $t^{0.5}$). MQ_{slope} quantifies the difference in propagation rate, while MQ_{offset} captures the vertical offset between the curves.

vertical intercepts of the respective regression lines and reflect the initial height offset between experiment and simulation.

These metrics quantify the accuracy of the simulated propagation rate and the initial lag between model and experiment. The observed offset is primarily attributed to transient wetting effects during material immersion, including initial lamella formation and meniscus curvature. Additional deviations may result from surface roughness, local porosity variations, or minor misalignments during experimental setup. While these short-term and localized phenomena are not resolved in the simulation, the model reliably captures the dominant in-plane propagation behavior over time. A detailed discussion of experimental variability and interpretation can be found in Kaden et al.^[70] While both metrics are reported, the parameter MQ_{slope} serves as the primary indicator for model quality. A classification scheme is applied to interpret model quality based on

$$\text{MQ} < 5\% \rightarrow \text{good} \quad (12)$$

$$5\% < \text{MQ} < 20\% \rightarrow \text{sufficient} \quad (13)$$

$$\text{MQ} > 20\% \rightarrow \text{insufficient} \quad (14)$$

2.2.4. Simulation Setup

After model parameterization, several different simulation configurations are used for validation, as described in Table 3.

2.2.4.1. Washburn Simulations for Individual Materials

A one-directional wetting setup is used to simulate the capillary rise of electrolyte in single materials. The simulation geometry mirrors the tensiometer setup, with boundary wetting applied from the bottom edge.^[70,71] These simulations are conducted for three selected materials (anode A1, separator S1, and cathode C1), with results compared to experimental measured data.

Table 3. Simulated cell geometries and wetting configurations. Each scenario is defined by the active area dimensions and the number and orientation of wetting fronts applied in the simulation setup.

Simulation name	Area [mm ²]	Wetting fronts
Washburn	40 × 20	1 (Bottom)
Washburn 1.4	70 × 50	1 (Bottom)
Cylindric 1.4	70 × 50	2 (Bottom & Up)
Cylindric 18 650	65 × 538.5	2 (Bottom & Up)
Cylindric 21 700	70 × 500	2 (Bottom & Up)
Pouch 1.4	70 × 50	4 (Around)
Pouch 2.8	99 × 35.5	4 (Around)
Pouch 5.6	140 × 25	4 (Around)

2.2.4.2. Washburn Simulations for Multilayer ESC

To investigate wetting dynamics across material interfaces, additional simulations are carried out for multilayer ESC configurations. These include bilayer and trilayer arrangements composed of previously characterized materials. Wetting rates are assigned based on experimentally measured data, either as direct values or as superpositions depending on the modeling assumption. The simulation setup enables the evaluation of inter-material wetting behavior and supports model extension toward full cell-level simulations.

2.2.4.3. Cell Simulations

Beyond the validation and multilayer investigations, the model was extended to simulate complete cell-level wetting scenarios. Two archetypical configurations have been considered: a stacked pouch cell and a wound cylindrical cell. For the pouch design, we implemented a four-front wetting setup, while the wound-cell design was approximated by a two-front configuration from the top and bottom edges.

To evaluate the influence of cell geometry, we tested different aspect ratios (AR = length/width) while maintaining a constant internal area (3500 mm²), reflecting cells of comparable capacity (\approx 1450 mAh with ten cathode layers). The investigated pouch geometries include AR = 1.4, 2.8, and 5.6. For each pouch cell geometry, four-front wetting was assumed. In addition, a one- and two-front wetting configuration was tested for AR = 1.4 to quantify the effect of wetting directionality. Furthermore, realistic cell formats based on 18 650 and 21 700 cylindrical cells were simulated using two-front wetting from both ends. These cases mirror the radial wetting behavior during actual cell filling processes, with heights set to 65 mm and 70 mm, respectively.

Across all configurations, the model calculated the physical time required for complete saturation, $t_{\text{simulated}}$. Additionally, we documented the actual computational run-time, t_{computed} . This has enabled the evaluation of the model's suitability for real-time integration into production control systems.

2.3. Experimental Validation Data

The data used to validate the simulation model—including the wetting rates and time-resolved measurement curves ($h \cdot t^{0.5}$)—were taken from the experimental study by Kaden et al.^[70] This publication also provides a comprehensive characterization of the materials used, including their porosity, thickness, and other parameters. In these experiments, the mass-based penetration rate K [g s^{-0.5}] was determined using a tensiometer setup (DATAPHYSICS INSTRUMENTS GMBH) for a wide range of individual electrode and separator materials, and their multilayer combinations were experimentally characterized. In the present work, we focused on a representative subset of these materials: one graphite-based anode (A1), one NMC622-based cathode (C1), and one ceramic-coated nonwoven separator (S1), as well as all bi- and trilayer combinations of these three materials. These introduced material designations follow the nomenclature introduced in Kaden et al. to ensure consistency and traceability of results.

The conversion of penetration rates K into wetting rates k for single-material measurements is performed by normalizing over the material properties according to Equation (15)

$$k = \frac{K}{A \cdot \Phi \cdot \rho} \quad (15)$$

Here, A represents the cross-sectional area, Φ the porosity of the solid structure, and ρ the density of the liquid. For multilayer samples, the conversion must account for the combination of different material layers. The superposed wetting rate \hat{k} is calculated using Equation (16), in which the conversion factor ζ is based on the sum of the surface areas \hat{A} and the averaged porosity $\hat{\Phi}$. The averaging of porosity is weighted by the area of each layer i .

$$\hat{k} = \frac{\hat{K}}{\zeta} = \frac{\hat{K}}{\rho \cdot \hat{A} \cdot \hat{\Phi}} = \frac{\hat{K}}{\rho \cdot \sum_i A_i \cdot \frac{\sum_i A_i \cdot \Phi_i}{\sum_i A_i}} \quad (16)$$

All wetting rates—both for individual materials and multilayer combinations—are derived using these formulae and serve as the basis for validating the simulation model presented in this work. An overview of the values can be found in Supporting Information Table S1.

3. Results and Discussion

3.1. Model Parameterization

To identify an optimal set of simulation parameters, we conducted a structured model calibration based on a reference scenario using the anode material A1. The three primary parameters examined were the spatial resolution l_{incr} , the maximum wetting rate k_{max} , and the threshold value T .

This parameter identification does not yet constitute a full model validation, but rather a calibration using a well-

characterized reference material. The actual validation of model generalizability is presented in the subsequent sections through comparison with independent experimental data for additional materials and multilayer configurations.

3.1.1. Spatial Grid Resolution and Maximum Wetting Rate

A full factorial variation of l_{incr} and k_{max} was performed to determine their impact on model accuracy by means of Err_{cum} and runtime. The results revealed that finer grid resolutions improve model fidelity, while smaller values of k_{max} reduce numerical overflow but increase simulation time.

As shown in Supporting Information Figure S3, a balanced trade-off was achieved at a spatial resolution $l_{\text{incr}} = 7 \times 10^{-5} \text{ mm lu}^{-1}$ and a maximum wetting rate $k_{\text{max}} = 8 \times 10^{-3} \text{ lu tu}^{-1}$. This configuration was selected for all Washburn simulations due to its sufficiently low error combined with reasonable computational demand. Due to the significantly larger modeled area in the cell simulations, the spatial discretization l_{incr} was selected as $2 \times 10^{-4} \text{ mm lu}^{-1}$.

3.1.2. Threshold Parameter

The threshold value determines when a cell becomes active in propagating electrolyte to its neighbors. A systematic variation revealed a strong influence of this parameter on the resulting wetting dynamics. As presented in Supporting Information Figure S4 and Table S5, the best agreement with the analytical reference model was achieved at a threshold value of 2/3, which yielded the lowest cumulative error.

3.2. Simulation Results and Discussion

3.2.1. Validation at Material Level

To validate the core functionality of the model, simulations were carried out for three representative materials: anode A1, cathode C1, and separator S1. Each simulation mimicked the 1D wetting geometry used in the tensiometer experiments, with boundary wetting applied from the bottom edge.

Quantitative comparisons of the simulated and experimental results for all three materials are presented in the first row of Figure 3. The model predictions for wetting height show strong agreement with the experimental curves. In all three cases, the simulation successfully replicates both the slope of the curve, which reflects the capillary-driven wetting rate, and the general shape of the wetting front.

The observed near-linearity of the wetting curves and the relatively smooth propagation front (Figure 4) are a result of the symmetric 1D experimental setup and the homogeneous properties of the reference material. The simulation assumes ideal boundary conditions and isotropic pore geometry, which reflect the actual behavior of material A1. Slight deviations near the lateral boundaries arise from geometric constraints in the Moore neighborhood, but these edge effects diminish with increasing

grid resolution and become negligible beyond 14 grid points from the edge.

To further evaluate model quality, the metrics MQ_{slope} and $\text{MQ}_{\text{offset}}$ were calculated. As summarized in Table 4, the slope deviation for all three materials remains below 5%, indicating high model fidelity. The offset for the anode and cathode remains below 1 mm, while the separator shows a higher deviation due to a longer initial swelling phase and slower initial uptake. This deviation is primarily attributed to experimental limitations and does not indicate a modeling error.

These results confirm that the CA model accurately captures the intramaterial electrolyte propagation across a variety of ESC materials and can be investigated further for the usage in extended simulations.

3.2.2. Validation of Multilayer ESC Simulations

Following the material-level validation, we extended the model to simulate multilayer ESC structures. In this approach, the wetting rates of the constituent materials were used as input parameters for stacked bilayer and trilayer configurations. Simulations were carried out using both superposition-based wetting rates (Simulation D) and interaction-adjusted wetting rates (Simulation I), allowing for a direct comparison of modeling strategies.

The second and third rows of Figure 3 illustrate the results for three representative bilayer cases: A1-A1, C1-C1, and A1-C1. While the superposition-based simulations systematically underestimated the wetting behavior, the simulations incorporating intermaterial interaction effects showed excellent agreement with experimental observations.

To evaluate the model's performance in more complex systems, the usage for trilayer configurations was analyzed. The results are shown in Figure 3 for the combinations A1-S1-A1, C1-S1-C1, and A1-S1-C1. As with the bilayer cases, only simulations that accounted for interaction effects accurately reproduced the experimental wetting curves. The superposition-based simulations again showed significant underprediction of the wetting dynamics, especially in asymmetric structures such as A1-S1-C1, where differing material properties and interfaces strongly influence the wetting progression.

This improved accuracy is quantified in Table 5, which compares the MQ_{slope} metric for both modeling approaches. Across all tested configurations, bi- and trilayer, simulations using interaction-based wetting rates achieved deviations of less than 5%, while superposition-based approaches deviated by 40%–60%. These results underscore the necessity of considering intermaterial interaction effects for accurate wetting prediction in composite systems.

3.2.3. Cell-Level Simulation and Runtime Feasibility

To assess the model's scalability and applicability in realistic cell geometries, we performed simulations across nine configurations

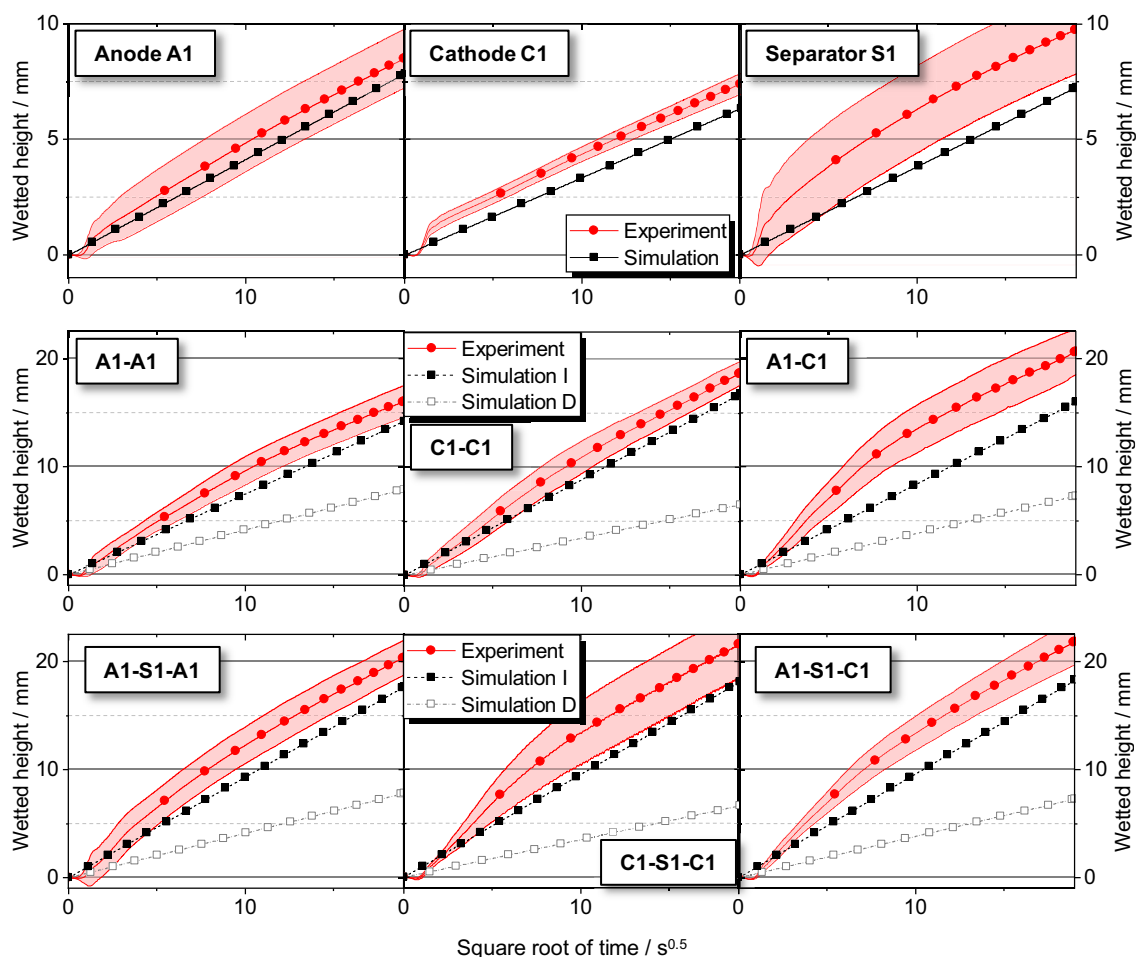


Figure 3. Comparison of experimental and simulated wetting heights over the square root of time for anode A1, cathode C1, and separator S1. Each plot shows the mean experimental data with standard deviation (shaded area) and the simulation results using the validated parameter set. Simulated and experimental wetting heights for multilayer configurations. Simulation results are shown for both superposition-based wetting rates (Simulation D) and rates including interaction effects (Simulation I).

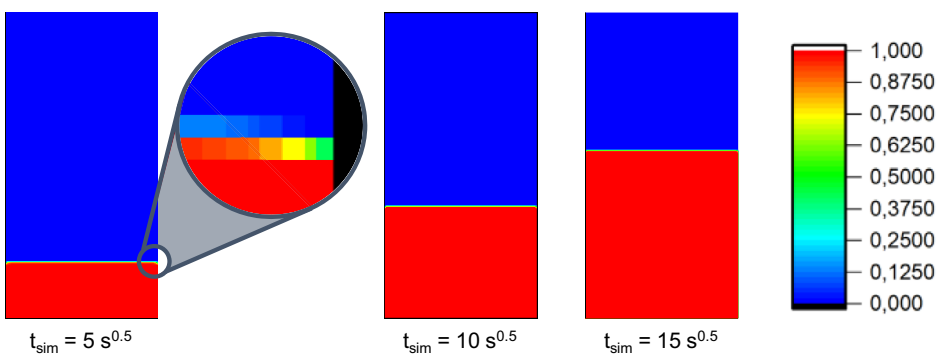


Figure 4. Qualitative simulation results for anode A1 at three time steps (early, mid, late). The color scale represents the local saturation state from 0 (dry, blue) to 1 (fully saturated, red). A zoomed section illustrates edge effects due to the Moore neighborhood, which lead to slower filling near corners. These effects become negligible with increasing grid resolution.

encompassing pouch, cylindrical, and Washburn test cases with varying wetting front numbers and aspect ratios. As shown in Table 6, the simulated saturation time $t_{\text{simulated}}$ varied depending on geometry and wetting setup. Notably, multifront wetting significantly reduced filling time compared to one- or two-front

configurations, due to shorter diffusion pathways in combination with the degressive decrease in wetting velocity over time (Washburn 1.4 vs. Cylindrical 1.4 vs. Pouch 1.4).

In addition to geometric effects, the influence of spatial resolution was evaluated using two Washburn simulations with

Table 4. Results of the intramaterial simulation validation based on the experimental tests with classification of the model quality into the categories MQ < 5% = good; 5% < MQ < 20% = sufficient; 20% < MQ = insufficient.

Number	MQ _{Slope} [%]	MQ _{Offset} [mm]	Evaluation of the MQ
A1	0.2	0.726	good
C1	2.3	0.943	good
S1	4.3	2.336	good

Table 5. Model quality comparison (MQ_{Slope}) for bi- and trilayer configurations.

Number	MQ _{Slope I} [%]	MQ _{Slope D} [%]
A1-A1	0.6	44.0
C1-C1	0.8	60.7
A1-C1	3.7	52.7
A1-S1-A1	0.6	55.5
C1-S1-C1	1.8	62.7
A1-S1-C1	0.6	60.4

identical geometry but different grid resolutions. The simulation using the coarser resolution ($l_{incr} = 2 \times 10^{-4} \text{ mm lu}^{-1}$) yielded only a 1.68% difference in $t_{simulated}$ compared to the fine-resolution case ($l_{incr} = 7 \times 10^{-5} \text{ mm lu}^{-1}$), yet its computational runtime was reduced by 90.25%. This highlights the importance of resolution tuning for achieving optimal runtime without compromising accuracy. Compared to experimental saturation times, both simulations showed slight deviations (+205 s and +235 s, respectively). These deviations can be explained by an initial offset observed in the experimental measurements (Figure 3, third row, right column), which stems from early lamella spreading and edge wetting effects not accounted for in the model initialization.

Shorter diffusion paths not only lead to shorter physical wetting times (as also shown in Kaden et al.), but also significantly

Table 6. Simulated wetting and experimental durations $t_{simulated}$ and computational runtimes $t_{computed}$ for various cell configurations. All cell simulations were performed with a spatial resolution of $l_{incr} = 2 \times 10^{-4} \text{ mm lu}^{-1}$. For comparison, two Washburn simulations with identical geometry but differing resolution are included:
¹ $l_{incr} = 7 \times 10^{-5} \text{ mm lu}^{-1}$ and ² $l_{incr} = 2 \times 10^{-4} \text{ mm lu}^{-1}$.

Cell simulation	$t_{simulated}$ [s]	$t_{computed}$ [s]	$t_{experiment}$ [s]
Washburn ¹	1739.7	194.17	1534.6 ^[70]
Washburn ²	1768.9	18.94	1534.6 ^[70]
Washburn 1.4 ²	9363.5	62.75	—
Cylindrical 1.4	1348.0	26.85	—
Cylindrical 18 650	1163.3	222.93	—
Cylindrical 21 700	1348.0	177.98	—
Pouch 1.4	682.2	19.07	614.1 ^[72]
Pouch 2.8	343.4	11.73	566.1 ^[72]
Pouch 5.6	172.3	7.86	508.4 ^[72]

reduce the number of time steps required in the simulation, thereby lowering computation time.^[72] This effect is particularly pronounced in multifront configurations, where wetting progresses simultaneously from multiple directions. For example, the Pouch 1.4 configuration, which uses a four-front setup, exhibits a reduction of more than 50% in computational runtime compared to the single-front Washburn setup, even under identical area conditions. Comparison with experimental data confirms the simulation results for the Pouch 1.4 case (error: +68.1 s). In contrast, the pouch cell variants with increased aspect ratios (Pouch 2.8 and Pouch 5.6) exhibit larger deviations from the experimental reference (errors of -222 s and -336 s, respectively). These discrepancies may be attributed to differences in boundary conditions, such as vacuum and overpressure states during and after electrolyte injection in the experimental setup—effects not included in the current simulation model.

For cylindrical cell geometries, simulation runtimes can be further reduced by focusing only on the wetting-relevant radial dimension. Since the model operates in two dimensions, the total electrode length of wound cells does not affect simulation time (Cylindrical 1.4 vs. Cylindrical 21 700).

Runtime comparisons further demonstrate the model's computational efficiency: all simulations completed significantly faster than the simulated wetting time. For example, the simulation of a 21 700 cylindrical cell geometry, which predicted full saturation after ≈ 1348 s, required less than 180 s of computation time on a standard GPU workstation. Even the most demanding Washburn simulation with the highest spatial resolution and longest single-front propagation path ($t_{simulated} \approx 9363.5$ s) completed in just over one minute.

These findings confirm the feasibility of using the model for real-time monitoring and decision support. The model's ability to simulate complex wetting scenarios with high accuracy and low computational effort makes it highly suitable for inline-capable digital production systems.

In summary, the model not only reproduces intramaterial wetting and accurately captures intermaterial propagation dynamics in multilayer configurations but also demonstrates its capability to simulate complete cell geometries under realistic conditions. The comparison between physical wetting durations and simulation runtimes confirms the model's suitability for real-time applications. These findings establish a strong foundation for further integration into digital battery production systems, enabling predictive process control and adaptive decision-making when planning or adapting new cell designs and formats, or when using quality data from upstream processes.

4. Conclusion

This work has introduced a CA model for simulating electrolyte wetting in porous lithium-ion battery components. Parameterized with experimental data, the model accurately reproduces wetting dynamics in both single- and multilayer structures including interaction-adjusted wetting rates for realistic propagation behavior. For single layer materials, intramaterial

electrolyte propagation was successfully simulated across three different ESC materials with deviations below 5% compared to the prior experimental results, especially for the chosen anode A1. Similarly, multilayer ESC wetting simulations yield high congruency to the experimental investigations with interaction-based wetting rates as opposed to assumed superposition approaches with deviations of 40 to 60%. The further analyses through cell-level wetting simulation entail reduced wetting times with higher aspect ratio and low discrepancies to experimental results when simulating different multifront wetting configurations for pouch and cylindrical cells, considering simplified boundary conditions in e.g., differential pressure.

The model's computational efficiency was further demonstrated through full cell simulations, proving high accuracy and simulation speeds for complex pouch and cylindrical formats surpassing real wetting times. The computational speed and accuracy confirm the model's applicability for real-time process control.

In further examinations, the model should be extended to 3D configurations to better consider spatially resolved wetting paths and interfacial effects and to simulatively support the simplified 2D assumptions. Additionally, the impact of design structures and manufacturing-induced defects could be explored further to increase the accuracy of the predictions. Of particular interest is the extension and inclusion of production process parameters such as temperature or pressures to increase the predictive power of the model. These developments could further enhance the model's utility for predictive quality assurance and digital twin applications in battery production.

Acknowledgements

This research was funded by the German Federal Ministry of Education and Research (BMBF) within the research project Cell-Fill (grant no. 03XP0237A) and ViPro (grant no. 03XP0324B). Cell-Fill investigated different parameters influencing wetting, innovative filling processes and measurement methods, as well as simulation models for dispensing and wetting. ViPro proposed a Cross Process Control architecture to model and predict the quality of processes in the battery production process chain such as the filling and subsequent wetting process. The predictions were used to adapt process parameters to reduce the number of rejects. The authors acknowledge support by the Open Access Publication Funds of Technische Universität Braunschweig.

Open Access funding enabled and organized by Projekt DEAL.

Conflict of Interest

The authors declare no conflict of interest.

Author Contributions

The authors confirm the absence of any undisclosed conflict of interest. **Nicolaj Kaden:** conceptualization (lead); formal analysis;

investigation; methodology; software (supporting); visualization; writing—original draft preparation (lead). **Jincui Cheng:** software (lead); writing—original draft preparation (supporting); **Benjamin Schumann:** conceptualization (supporting); software (supporting); writing—original draft preparation (supporting). **Do Minh Nguyen:** validation (equal) and writing—review and editing (equal). **Ricarda Schlimbach:** validation (equal) and writing—review and editing (equal); and **Klaus Dröder:** project administration, resources, supervision and writing—review and editing (equal). All authors have read and agreed to the published version of the manuscript.

Data Availability Statement

Selected datasets and materials that support the findings of this study are available from the corresponding author upon reasonable request.

Keywords: battery manufacturing • cellular automaton • electrolyte filling • lithium-ion battery • wetting simulation model

- [1] X. Guo, K. Huang, L. Li, X. Wang, *Sustainability* **2023**, *15*, 234.
- [2] B. Szetela, A. Majewska, P. Jamroz, B. Djalilov, R. Salahodjaev, *Front. Energy Res.* **2022**, *10*, 872941.
- [3] R. Ochoa-Barragán, J. M. Ponce-Ortega, J. Tovar-Facio, *Sustain. Prod. Consum.* **2023**, *42*, 335.
- [4] J. Flesischmann, P. Schaufuss, M. Lindner, M. Hanicke, E. Horetsky, D. Ibrahim, S. Jautelat, L. Torsch, A. van de Rijt, *McKinsey Company* **2023**, *16*, 2023.
- [5] B. Scrosati, J. Garche, *J. Power Sources* **2010**, *195*, 2419.
- [6] K. Liu, Y. Liu, D. Lin, A. Pei, Y. Cui, *Sci. Adv.* **2018**, *4*, eaas9820.
- [7] Y. Chen, Y. Kang, Y. Zhao, L. Wang, J. Liu, Y. Li, Z. Liang, X. He, X. Li, N. Tavajohi, B. Li, *J. Energy Chem.* **2021**, *59*, 83.
- [8] S. Mahmud, M. Rahman, M. Kamruzzaman, M. O. Ali, M. S. A. Emon, H. Khutun, M. R. Ali, *Results Eng.* **2022**, *15*, 100472.
- [9] D. L. Wood, J. Li, C. Daniel, *J. Power Sources* **2015**, *275*, 234.
- [10] S. Feng, C. L. Magee, *Appl. Energy* **2020**, *260*, 114264.
- [11] J.-H. Schünemann (2015) Modell zur Bewertung der Herstellkosten von Lithiumionenbatteriezellen. TU Braunschweig. Dissertation.
- [12] A. Kampker, H. Heimes, B. Dorn, C. Offermanns, M. Frieges, S. Wennemar, D. Neb, N. Kisseler, M. Drescher, J. Gorsch, B. Späth, N. Lackner, W. Bernhart, J.-P. Hasenberg, T. Hotz, D. Gallus, K. Knoche, I. Demir, T. Achmadeev, *Battery Monitor* **2023**: The Value Chain Between Economy And Ecology, PEM of RWTH Aachen University, Aachen, Germany 2023.
- [13] M. Wentker, M. Greenwood, J. Leker, *Energies* **2019**, *12*, 504.
- [14] G. Berckmans, M. Messagie, J. Smekens, N. Omar, L. Vanhaverbeke, J. van Mierlo, *Energies* **2017**, *10*, 1314.
- [15] S. Orangi, A. H. Strømman, *Batteries* **2022**, *8*, 83.
- [16] Y. Liu, R. Zhang, J. Wang, Y. Wang, *iScience* **2021**, *24*, 102332.
- [17] F. Duffner, L. Mauler, M. Wentker, J. Leker, M. Winter, *Int. J. Prod. Econ.* **2021**, *232*, 107982.
- [18] F. Schomburg, B. Heidrich, S. Wennemar, R. Drees, T. Roth, M. Kurrat, H. Heimes, A. Jossen, M. Winter, J. Y. Cheong, F. Röder, *Energy Environ. Sci.* **2024**, *17*, 2686.
- [19] N. Kaden, R. Schlimbach, Á. Rohde García, K. Dröder, *Batteries* **2023**, *9*, 164.
- [20] J. Cannarella, C. B. Arnold, *J. Electrochem. Soc.* **2015**, *162*, A1365.
- [21] J. Hagemeister, S. Stock, M. Linke, M. Fischer, R. Drees, M. Kurrat, R. Daub, *Energy Tech* **2023**, *11*, 2200686.
- [22] M. P. Lautenschlaeger, B. Priffling, B. Kellers, J. Weinmiller, T. Danner, V. Schmidt, A. Latz, *Batteries Supercaps* **2022**, *5*, e202200090.
- [23] J. Hagemeister, A. Elkoshesh, Y. Hu, R. Daub, *Procedia CIRP* **2024**, *126*, 841.
- [24] D. H. Jeon, *Trans. Korean Soc. Mech. Eng. B* **2016**, *40*, 47.
- [25] D. H. Jeon, *Appl. Mater. Today* **2021**, *22*, 100976.
- [26] S. G. Lee, D. H. Jeon, *J. Power Sources* **2014**, *265*, 363.

- [27] D. H. Jeon, *Energy Storage Mater.* **2019**, *18*, 139.
- [28] S. G. Lee, D. H. Jeon, B. M. Kim, J. H. Kang, C.-J. Kim, *J. Electrochem. Soc.* **2013**, *160*, H258.
- [29] D. H. Jeon, J.-H. Song, J. Yun, J.-W. Lee, *ACS nano* **2022**, *17*, 1305.
- [30] J. Wanner, K. P. Birke, *Batteries* **2022**, *8*, 277.
- [31] J. Wanner, K. P. Birke, *Energies* **2023**, *16*, 5640.
- [32] J. Wanner, K. P. Birke, *J. Energy Storage* **2024**, *87*, 111410.
- [33] J. Wanner, M. Burgard, N. Othman, S. Singh, K. P. Birke, *Batteries Supercaps* **2024**, *8*, e202400531.
- [34] M. P. Lautenschlaeger, J. Weinmiller, B. Kellers, T. Danner, A. Latz, *Adv. Water Resour.* **2022**, *170*, 104320.
- [35] A. Shodiev, E. Primo, O. Arcelus, M. Chouchane, M. Osenberg, A. Hilger, I. Manke, J. Li, A. A. Franco, *Energy Storage Mater.* **2021**, *38*, 80.
- [36] A. Shodiev, F. M. Zanotto, J. Yu, M. Chouchane, J. Li, A. A. Franco, *Energy Storage Mater.* **2022**, *49*, 268.
- [37] M. Abubaker, C. H. Sohn, H. M. Ali, *Energy Rep.* **2024**, *11*, 2333.
- [38] M. Abubaker, C.-H. Sohn, H. M. Ali, *J. Therm. Anal. Calorim.* **2024**, *149*, 1.
- [39] M. Abubaker, C.-H. Sohn, H. M. Ali, *Energy Rep.* **2024**, *12*, 2548.
- [40] S. K. Mohammadian, Y. Zhang, *Int. J. Heat Mass Transf.* **2018**, *118*, 911.
- [41] F. Chen, T. Chen, Z. Wu, Z. Zhou, K. Lu, J. Su, Y. Wang, J. Hua, X. Lai, X. Han, M. Ouyang, Y. Zheng, *Green Energy Intell. Transp.* **2025**, *4*, 100248.
- [42] H.-S. Chen, S. Yang, W.-L. Song, Le Yang, X. Guo, X.-G. Yang, N. Li, D. Fang, *eTransportation* **2023**, *16*, 100232.
- [43] J. Y. Cho, H. M. Lee, J. H. Kim, W. Lee, J. S. Lee, *Eng. Appl. Comput. Fluid Mech.* **2022**, *16*, 177.
- [44] A. El Malki, M. Asch, O. Arcelus, A. Shodiev, J. Yu, A. A. Franco, *J. Power Sources Adv.* **2023**, *20*, 100114.
- [45] A. Shodiev, M. Duquesnoy, O. Arcelus, M. Chouchane, J. Li, A. A. Franco, *J. Power Sources* **2021**, *511*, 230384.
- [46] S. Stock, S. Pohlmann, F. J. Günter, L. Hille, J. Hagemeister, G. Reinhart, *J. Energy Storage* **2022**, *50*, 104144.
- [47] J. Schnell, C. Nentwich, F. Endres, A. Kollenda, F. Distel, T. Knoche, G. Reinhart, *J. Power Sources* **2019**, *413*, 360.
- [48] M. Schönenemann, H. Bockholt, S. Thiede, A. Kwade, C. Herrmann, *Int. J. Adv. Manuf. Technol.* **2019**, *102*, 1373.
- [49] M. Dent, S. Grabe, C. Lekakou, *Batteries Supercaps* **2024**, *7*, e202300327.
- [50] T. Neumann, K. Boettcher, P. Ehrhard, *Proc. Appl. Math. Mech.* **2017**, *17*, 659.
- [51] C. Sauter, R. Zahn, V. Wood, *J. Electrochem. Soc.* **2020**, *167*, 100546.
- [52] S. Shin, H. Kim, T. Maiyalagan, S. Chul Yi, *Mater. Sci. Eng.: B* **2022**, *284*, 115878.
- [53] F. L. E. Usseglio-Viretta, P. J. Weddle, B. J. Tremolet de Villers, N. Dunlap, D. Kern, K. Smith, D. P. Finegan, *J. Electrochem. Soc.* **2023**, *170*, 120506.
- [54] A. Davoodabadi, J. Li, Y. Liang, D. L. Wood, T. J. Singler, C. Jin, *J. Power Sources* **2019**, *424*, 193.
- [55] M. Gebrekirnos Berhe, H. G. Oh, S.-K. Park, M. Mondal, D. Lee, *Mater. Des.* **2023**, *231*, 112020.
- [56] J. Wanner, M. Weeber, K. P. Birke, A. Sauer, *Procedia CIRP* **2023**, *118*, 987.
- [57] N. Fries, M. Dreyer, *J. colloid Interface Sci.* **2008**, *320*, 259.
- [58] F. J. Günter, J. Keilhofer, C. Rauch, S. Rössler, M. Schulz, W. Braunwarth, R. Gilles, R. Daub, G. Reinhart, *J. Power Sources* **2022**, *517*, 230668.
- [59] J. Hagemeister, A. Elkoshet, A. Yakici, F. Günter, Y. Hu, R. Daub, *Energy Tech* **2024**, *13*, 2401708.
- [60] T. Neumann, K. Boettcher, P. Ehrhard, *Proc. Appl. Math. Mech.* **2016**, *16*, 605.
- [61] J. Meiners, A. Fröhlich, K. Dröder, *Procedia CIRP* **2022**, *112*, 525.
- [62] Anthony D. Rhodes (2013) The Algebraic Structure of Cellular Automata.
- [63] H. Sayama, *Introduction To The Modeling And Analysis Of Complex Systems*, Open SUNY Textbooks, Milne Library, Geneseo, NY **2015**.
- [64] D. Adalsteinsson, M. Hilpert, *Transp. Porous. Med.* **2006**, *65*, 337.
- [65] M. Hilpert, C. T. Müller, *Adv. Water Resour.* **2001**, *24*, 243.
- [66] J. Kmec, T. Fürst, R. Vodák, M. Šír, *Sci. Rep.* **2021**, *11*, 3223.
- [67] C. Chang, C.-H. Liu, C.-A. Lin, *Comput. Math. Appl.* **2009**, *58*, 940.
- [68] E. W. Washburn, *Phys. Rev.* **1921**, *17*, 273.
- [69] N. Kaden, D. M. Nguyen, R. Schlimbach, T. Ohnimus, A. Kwade, K. Dröder, *J. Power Sources* **2024**, *621*, 235282.
- [70] N. Kaden, N. Schlüter, R. Leithoff, S. Savas, S. Grundmeier, K. Dröder, *Processes* **2021**, *9*, 1851.
- [71] N. Kaden, W. Guo, M. Göhrmann, T. Koch, J. Cheng, D. M. Nguyen, R. Schlimbach, K. Dröder, *Energy Tech* **2025**, *13*, 2401338.
- [72] F. J. Günter, J. Keilhofer, V. Böhm, R. Daub, G. Reinhart, *J. Electrochem. Soc.* **2022**, *169*, 50522.
- [73] J. Hagemeister, F. J. Günter, T. Rinner, F. Zhu, A. Papst, R. Daub, *Batteries* **2022**, *8*, 159.
- [74] T. Knoche, F. Surek, G. Reinhart, *Procedia CIRP* **2016**, *41*, 405.

Manuscript received: May 9, 2025

Revised manuscript received: June 3, 2025

Version of record online: